

Spectroscopy and nonlinear microscopy of gold nanoparticle arrays on gold films

Andreas Hohenau and Joachim R. Krenn

Karl-Franzens University and Erwin Schrödinger Institute for Nanoscale Research, A-8010 Graz, Austria

Francisco J. Garcia-Vidal

Departamento de Física Teórica de la Materia Condensada, Universidad Autónoma de Madrid, E-28049 Madrid, Spain

Sergio G. Rodrigo and Luis Martín-Moreno

Departamento de Física de la Materia Condensada, ICMA-CSIC, Universidad de Zaragoza, E-50009 Zaragoza, Spain

Jonas Beermann and Sergey I. Bozhevolnyi

Department of Physics and Nanotechnology, Aalborg University, DK-9220 Aalborg Øst, Denmark

(Received 2 November 2006; published 8 February 2007)

Regular arrays of rectangular gold nanoparticles placed on gold films are characterized by using linear reflection spectroscopy (in the wavelength range of 450–950 nm) and nonlinear scanning optical microscopy, in which two-photon photoluminescence (TPL) excited with a strongly focused laser beam (in the wavelength range of 730–820 nm) is detected. Experimental results are modeled using a finite-difference time-domain approach with the dielectric function of gold approximated by a Drude-Lorentz formula, showing a rather good agreement between the experimental and theoretical reflection and TPL enhancement spectra. The modeling is also used to optimize the array parameters for achieving strong and well-pronounced TPL enhancement maxima in the wavelength range accessible to the used experimental techniques, i.e., close to 800 nm. Accordingly designed samples are fabricated and characterized, corroborating the modeling predictions. We discuss the origin of TPL enhancement and its relation to local-field enhancements at the sample surface as well as its characterization with TPL microscopy. The implications of the obtained results are also discussed.

DOI: [10.1103/PhysRevB.75.085104](https://doi.org/10.1103/PhysRevB.75.085104)

PACS number(s): 42.65.-k, 73.20.Mf, 02.70.Bf

I. INTRODUCTION

Light scattering by arrays of metal nanoparticles gives rise to nanostructured optical fields exhibiting strong and spatially localized (on a nanometer scale) field intensity enhancements that play a major role in various surface enhanced phenomena. The local field enhancement effects are of high interest, in general, for fundamental optics and electrodynamics¹ and for various applied research areas, such as surface-enhanced Raman spectroscopy² and microscopy including optical characterization of individual molecules.³ Individual metal particles can exhibit optical resonances associated with resonant collective electron oscillations known as localized surface plasmons (LSPs).⁴ Excitation of LSPs results in the occurrence of pronounced bands in extinction and reflection spectra and in local-field enhancement effects. These effects can be further enhanced due to resonant interactions between particles arranged in a periodic array. For metal particles placed on a metal surface, interparticle interactions can be mediated by surface electromagnetic excitations bound to metal-dielectric interfaces, i.e., by surface plasmon polaritons (SPPs),⁵ whose resonant excitation can be achieved by tuning the array periodicity.

The search for configurations ensuring reliable realizations of strongly enhanced local fields is often conducted with the help of linear extinction and/or reflection spectroscopy, where minima in the transmitted and/or reflected light intensity are associated with the excitation of system resonances (see Ref. 6 and references therein). This characterization technique is considered reliable but lacking spatial resolution, since the spectra are influenced by a whole

illuminated area containing many nanoparticles. In addition, the information obtained is not direct since the relation between the extinction and/or reflection minima and local-field enhancements is rather complicated. For example, the extinction is determined not only by the absorption and scattering of individual particles but also by the scattering diagram of a given particle array.⁷ A more direct approach for the evaluation of local-field intensity enhancement has been recently developed utilizing two-photon excited luminescence in gold.⁸ This technique is based on the circumstance that strongly enhanced local fields due to the excitation of LSPs in gold nanostructures give rise to two-photon absorption, which in turn leads to a broad emission continuum (generated by interband transitions of *d*-band electrons into the conduction band) known as two-photon excited (photo) luminescence (TPL) in gold.⁹ It has been demonstrated that nonlinear scanning optical microscopy, in which the TPL excited with a strongly focused laser beam is detected, can be used for the characterization of the local-field intensity enhancement in gold nanoparticles (bow-tie nanoantennas) and at their surfaces.⁸ We have recently applied linear extinction spectroscopy, TPL microscopy, and theoretical modeling based on the finite-difference time-domain (FDTD) method to study arrays of gold nanoparticles on glass substrates.¹⁰ In general, we have found good correspondence between the results obtained in the experiments and simulations, indicating the reliability of the developed modeling approach for adequately describing both experimental techniques.

In this work, we apply the techniques of reflection spectroscopy and TPL microscopy along with the FDTD modeling¹⁰ to studies of gold nanoparticle arrays placed on a

gold surface, aiming at optimizing the array geometry for TPL enhancement and elucidating the roles played by LSP and SPP resonances in local-field enhancement effects as well as gaining further insight into the electro-dynamical processes involved in TPL generation. The paper is organized as follows. In Sec. II, the investigated arrays are described and the characterization techniques are outlined, followed by a brief description of the modeling approach used. Section 3 presents the obtained results and their discussion, starting with the comparison of measured and simulated reflection spectra for different array periods and sizes of gold nanoparticles. The ensuing discussion is supported with the field intensity distributions calculated at different cross sections of an individual particle. The modeling is then used to optimize the array parameters for achieving strong resonances (and local-field enhancements) in the wavelength range of TPL microscopy, and the corresponding results obtained with both characterization techniques are presented and discussed. We offer our conclusions in Sec. IV that terminates the paper.

II. SAMPLE DESCRIPTION AND METHODS

A. Experiment

The samples consist of two-dimensional arrays of nominally rectangular, 50-nm-high gold particles on top of a 55-nm-thick gold film on a glass substrate [inset of Fig. 1(b)] produced by electron-beam lithography.¹¹ The overall size of the arrays is $100 \times 100 \mu\text{m}^2$. The lateral dimensions of the particles and the grating constants of the arrays are varied to systematically study their influence on the optical extinction and reflection spectra and the TPL signal.

Reflection spectra are recorded by a Zeiss MMS-1 microspectrometer attached to a conventional optical microscope equipped with a $2.5\times$, 0.075 numerical aperture objective. To control the polarization, a polarizer is inserted in front of the spectrometer entrance. The reference for the reflection spectra was taken on the plain, unstructured gold film outside the areas covered with particle arrays. The spectra therefore directly reflect the optical properties of the particle arrays.

The experimental setup for TPL scanning microscopy (for details, see Ref. 12) allows us to simultaneously record the TPL signal (detected by a photomultiplier) and the backscattered light (detected by a photodiode) as a function of the sample position with the resolution determined by the focal spot size of the excitation laser at the sample surface ($\sim 1 \mu\text{m}$).¹³ For excitation, we use a 200 fs Ti:sapphire laser at a repetition rate of 80 MHz with a linewidth of ~ 10 nm and an adjustable polarization plane. The laser wavelength can be tuned between 720 and 900 nm, which allows us to make spectrally resolved studies of TPL efficiency. The typical average incident power is in the range of 0.1–50 mW.

B. Simulations

For FDTD simulations, we modeled the samples as gold particles on top of a 55-nm-thick gold film on a semi-ininitely extending glass substrate. Similar to our previous work,¹⁰ the fields were calculated in a box of $\Lambda_x \times \Lambda_y$

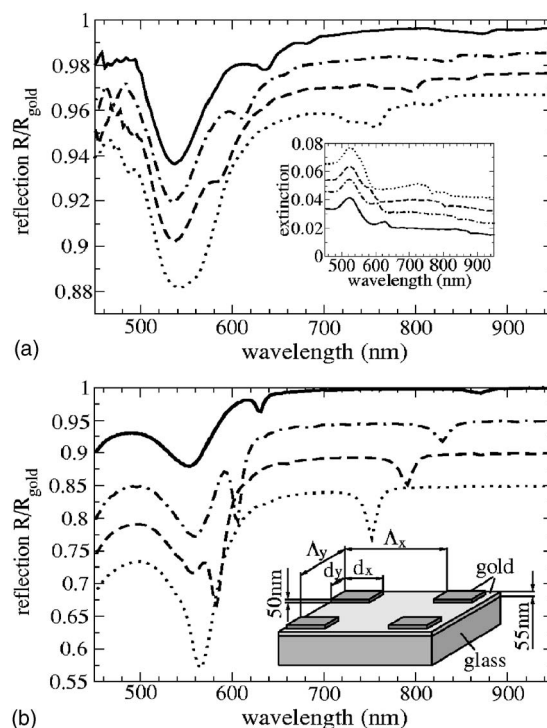


FIG. 1. (a) Measured and (b) calculated reflection spectra of particle arrays of square gold particles ($d_x=d_y=150$ nm, height $d_z=50$ nm) on a 55-nm-thick gold film on top of glass [see the inset in (b)] for different array periods: $\Lambda_x=\Lambda_y=860$ nm (solid line), $\Lambda_x=\Lambda_y=820$ nm (dash-dotted line), $\Lambda_x=\Lambda_y=780$ nm (dashed line), and $\Lambda_x=\Lambda_y=740$ nm (dotted line). The curves are vertically offset for clarity. The inset in (a) depicts the measured extinction spectra, which show features at the same spectral position as observed in the reflection spectra. The spectra are identical for x and y polarization.

$\times 1.3 \mu\text{m}^3$ with periodic boundary conditions at the walls perpendicular to the substrate and a “uniaxial perfect matched layer”¹⁴ (PML) at the walls parallel to the substrate. Additionally, in this work concurrent complementary operators method¹⁵ (CCOM) layers were also added to the PML layers. The parameters defining the CCOM layers were chosen to be complementary to the PML layers. In this way, one can use thinner PML layers, and the energy flowing at grazing incidence is better absorbed. This is of special importance in the considered system, as small SPP peaks in reflection have to be resolved and small errors in the reflection of grazing modes due to unwanted lack of absorption by the absorbing layers could be spuriously attributed to SPP resonances.

Typically, the cell size was $5 \times 5 \times 5 \text{ nm}^3$ in space and the time steps were 0.0077 fs (corresponding to a Courant-Friedrich-Levy factor of 0.8) to guarantee the numerical stability of the simulations. After a simulation time of 100 fs, convergence was guaranteed. The dielectric function for gold was approximated by a Drude-Lorentz formula,^{10,15,16} and the structures were excited by a Gaussian wave packet composed of plane waves with the wave-vector \mathbf{k} perpendicular to the substrate and all frequencies of interest. Spectra were calculated after projection onto diffracted modes. Only the zero-order mode was considered in the postprocessing, as

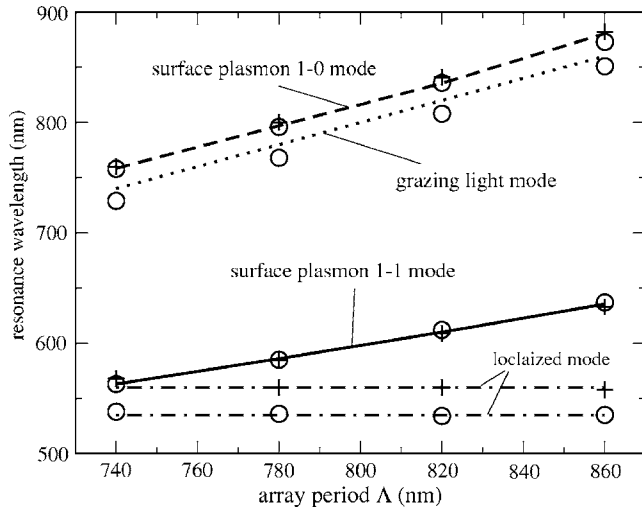


FIG. 2. Position of the different dips observed in the reflection spectra vs array period as measured from Fig. 1 (circles, experiment; crosses, simulation). The lines represent the expected dip positions for grating coupling to the [1 1] (solid line) and the [1 0] (dashed line) surface plasmon mode and the excitation of a grazing light mode (dotted line). The horizontal lines reflect the independence of a localized mode on the array period (dash-dotted lines).

experimental intensities were collected in a small solid angle centered around the normal direction.

III. RESULTS AND DISCUSSION

A. Reflection spectra

We first consider the far-field reflection spectra of the particle arrays to confirm that the FDTD method is applicable to this system and leads to results in reasonably good agreement with the experiment. Figure 1 depicts the experimentally recorded and FDTD simulated reflection spectra for arrays with particles of approximately $150 \times 150 \times 50 \text{ nm}^3$ in a square array with periods $\Lambda_x = \Lambda_y = 740, 780, 820,$ and 860 nm . Due to the symmetry of the arrays, spectra for x and y polarization look identical. In very good agreement between experiment and simulations, the reflection spectra display distinct features in three wavelength regions: (A) a single, broad reflection dip at $\sim 550 \text{ nm}$ independent of the array period, (B) a dip at the long-wavelength wing of the 550 nm dip, and (C) a dip (in the case of the experimental spectra with a shoulder $\sim 20 \text{ nm}$ to the blue of the dip) at a light wavelength close to the value of the array period ($740\text{--}860 \text{ nm}$). Whereas the independence of dip A on the array period points toward the excitation of a mode localized to the single particles, i.e., the LSP mode, the dip structures B and C clearly depend on the array period and can therefore be related to a coupling between the particles. A closer analysis of the spectral dip positions allows us to clarify their origin (Fig. 2). Dip C as well as dip B are exactly at the position expected for grating coupling to SPPs on the air-gold interface in the [1 0] and [1 1] modes (the SPP dispersion relation on the array is assumed to follow that of the SPP on an unstructured surface of a 55-nm -thick gold

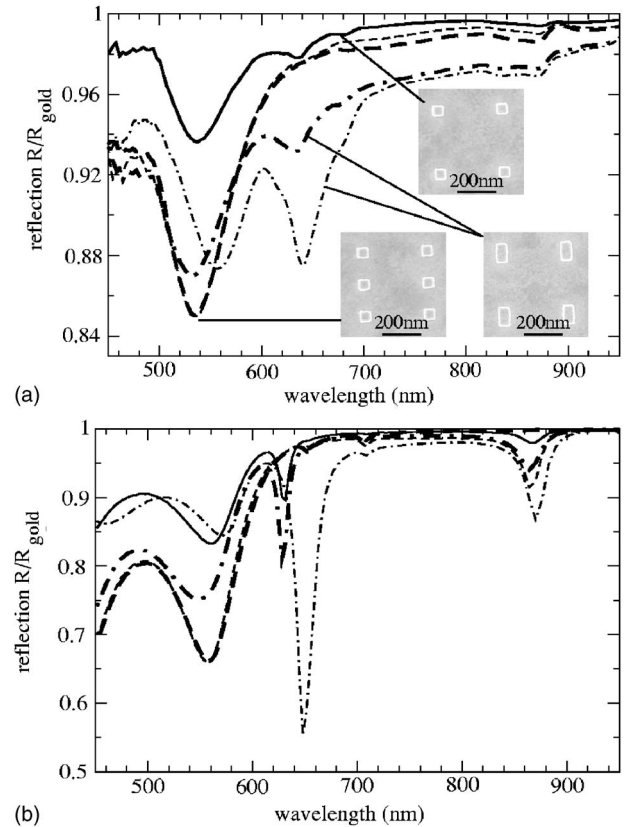


FIG. 3. (a) Measured and (b) calculated reflection spectra of particle arrays with $\Lambda_x = \Lambda_y = 860 \text{ nm}$ and $d_x = d_y = 150 \text{ nm}$ (solid line), $\Lambda_x = 2\Lambda_y = 860 \text{ nm}$ and $d_x = d_y = 150 \text{ nm}$ (thick and thin dashed lines for x and y polarization, respectively), and $\Lambda_x = \Lambda_y = 860 \text{ nm}$ and $d_x = \frac{1}{2}d_y = 150 \text{ nm}$ (thick and thin dash-dotted lines for x - and y -polarization, respectively). The particle height for all arrays is $d_z = 50 \text{ nm}$. The insets show electron micrographs of the corresponding arrays.

film¹⁷). The experimentally observed shoulder $\sim 20 \text{ nm}$ to the blue of dip C is, in turn, close to the spectral position expected for coupling to grazing grating orders in air. The slight blueshift of its observed spectral position compared to the “ideal” position is due to the far-field emission pattern of dipoles or multipoles above a plane interface, which show considerable strength only close to the grazing angle but are vanishing in the direction parallel to the interface.¹⁸ This shoulder appears much weaker in the simulations and is not discernible in Fig. 1(b). We assign this and the differences in dip width and strength between experiment and simulations to the unavoidable geometrical imperfections of the sample, the finite numerical aperture of the microscope objective, and the finite array size.

To gain information on the parameters which determine the spectral position and strength of the LSP resonance and the grating coupling dips, we produced and investigated samples with different particle shapes and array geometries. For example, rectangular particles created by either bisecting (not shown) or doubling (dash-dotted curves, Fig. 3) the y dimension of the particles lead to a slight splitting of the LSP resonance (peak A) for different polarizations. For the latter case, we observe a redshift ($\sim 20 \text{ nm}$) of the resonance for a

polarization parallel to the long particle axis (y polarization, thin dash-dotted curve in Fig. 3) and a blueshift (~ 5 nm) for a polarization parallel to the short particle axis (x polarization, thick dash-dotted curve in Fig. 3). In addition, for this polarization we experimentally find a comparably strong occurrence of dip B (grating coupling to the SPP along the $[1\ 1]$ direction) combined with a slight redshift. For polarization parallel to the long particle axis (y polarization), it seems that the efficiency of coupling to grating modes is enhanced, while the coupling to the LSP mode gets slightly weaker. These effects are reproduced by the simulations, but their origins remain to be clarified and require further study.

Finally, by bisecting the array period in the y direction ($\Lambda_x=2\Lambda_y=860$ nm), a complete suppression of the $[1\ 1]$ SPP modes can be demonstrated (dashed curves, Fig. 3). This effect can be qualitatively understood by considering the grating coupling mechanism and the optical properties of the gold film. The SPP wavelength determined by the grating mode and the array period (i.e., 385 nm for the $[1\ 1]$ mode) requires a frequency that is larger than the onset of the gold d -band absorption. SPPs excited within this absorption range are strongly damped and have propagation lengths smaller than their wavelengths and the grating periodicity. Consequently, no resonant grating excitation of these SPP modes can occur.

It is interesting to note the differences of the spectra of these arrays of gold particles on a 55-nm-thick gold film to the spectra of similar particles on a glass substrate.¹⁰ The spectra of the particles on the glass substrate are dominated by the (shape-dependent) LSP resonance of individual particles, whose strength and spectral width are influenced by the array in terms of suppression of different allowed or forbidden diffraction modes. In contrast, for the particles on the gold film, we find a LSP resonance whose spectral position only weakly depends on the particle shape and size (Fig. 3) and is always close to ~ 550 nm. Additionally, different features corresponding to grating coupling to SPPs on the gold-air interface and the excitation of grazing diffracted light modes in air occur. The spectral position of these features naturally depends mostly on the array period but, their strength can be influenced by the particle shape and size.

B. Optical near-field pattern

We now turn to the calculated optical near-field pattern and analyze them exemplarily for the array with $\Lambda_x=\Lambda_y=740$ nm and particle dimensions $d_x=d_y=150$ nm and height $d_z=50$ nm (compare Fig. 1). For this array, the LSP resonance and the $[1\ 1]$ SPP resonant excitation coincide spectrally, leading to an enhanced SPP excitation and, therefore, a stronger signature in the optical near fields.

We first consider the optical near-field intensities in an x - y plane at the surface of the gold film for illumination at the wavelengths of 563 nm [Fig. 4(a)] and 752 nm [Fig. 4(b)], corresponding to the resonant grating excitation of the $[1\ 1]$ and $[1\ 0]$ SPP modes, respectively. The images clearly show standing-wave patterns which result from the interference of the excited SPP modes and corroborate the interpretation derived from the spectra. In the first case (excitation at

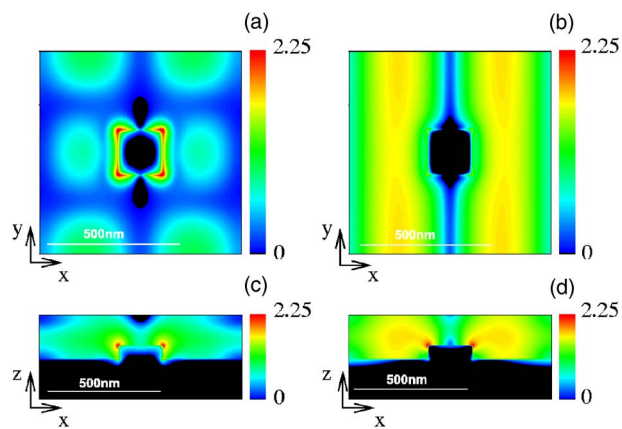


FIG. 4. (Color online) Calculated optical near-field images (plotted quantity: $\log(|E(\mathbf{r},\lambda)|^2/|E(\lambda)|^2)$, where $E(\mathbf{r},\lambda)$ is the electric-field amplitude of the array and $E(\lambda)$ is the electric-field amplitude in the top layer of a flat surface) for the array with $\Lambda_x=\Lambda_y=740$ nm and $d_x=d_y=150$ nm (extinction spectrum: Fig. 1, dotted line) in the x - y plane at the surface of the gold film when excited at (a) 563 nm ($[1\ 1]$ mode) and (b) 752 nm ($[1\ 0]$ mode), and corresponding images in the x - z plane through the particle center at (c) 563 nm and (d) 752 nm. The particle height is $d_z=50$ nm.

563 nm), four equivalent SPP modes are excited: $[1\ 1]$, $[1\ -1]$, $[-1\ 1]$, and $[-1\ -1]$. The interference of these four modes, which propagate in the diagonal directions leads to the characteristic pattern observed. Due to the partly longitudinal nature of the SPP field, no SPP modes propagating perpendicularly to the polarization direction of the incoming light can be excited.¹⁹ Therefore, in the case of the excitation at 752 nm (x polarization), only the $[1\ 0]$ and $[-1\ 0]$ SPP modes are excited, whose interference leads to a standing-wave pattern with wave fronts parallel to the y direction, as clearly observed in Fig. 4(b).

In both cases, the optical fields are vertically well-confined to the surface region [Figs. 4(c) and 4(d)], thereby manifesting their evanescent nature inherent to SPP modes. In addition to the SPP fields covering a large part of the array surface, strongly localized near fields are observed close to the upper edges of the particles in both cases [Figs. 4(c) and 4(d)]. These local-field enhancements are due to the lightning rod effect (i.e., field enhancements close to sharp tips or corners) being further enhanced in the first case due to the LSP resonance.

By comparing the near-field intensities just below and above the metal surface in the cross-cuts [Figs. 4(c) and 4(d)], one can realize the strong intensity jumps over the gold-air interface in some regions. This is related to the fundamental difference of the continuity condition for the electric-field components parallel and perpendicular to the interface. In regions where the electric field is mostly parallel to the metal-air interface, the fields are continuous across the interface. However, in regions where the electric field also has a considerable component vertical to the metal-air interface, this component is larger in air by the ratio of the dielectric constants of gold to air (for example, at 752 nm excitation $\epsilon_{\text{Au}} \approx -20.2 + 1.3i$, which can cause a maximum

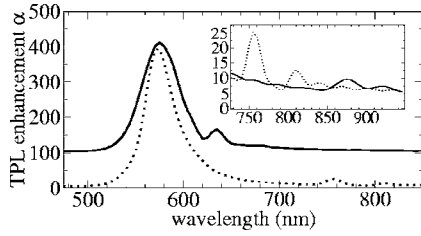


FIG. 5. Calculated TPL enhancement spectra for the arrays with $\Lambda_x=\Lambda_y=860$ nm and $d_x=d_y=150$ nm (solid line) and $\Lambda_x=\Lambda_y=740$ nm and $d_x=d_y=150$ nm (dotted line). For clarity, the curves are vertically offset by 100. The inset depicts a close-up of the spectral region of 735–950 nm (no offset between curves).

intensity jump of $|\epsilon_{\text{Au}}|^2 \approx 411$ in the case of an electric field purely perpendicular to the interface). This detail highlights the complementary nature of TPL signals, which probe the field inside the metal, vs other methods probing the near field (e.g., surface-enhanced Raman scattering or any type of optical near-field microscopy) just outside the metal.

C. Calculated TPL enhancement

For the calculation of the TPL enhancement, we assume that the TPL signal originates from the top layer of the gold array following the surface topography.¹⁰ The achievable TPL intensity enhancement factor $\alpha(\lambda)$ can be evaluated from the electric-field amplitudes E by

$$|\alpha|^2(\lambda) = \frac{\int \int_{A_{\text{cell}}} |E(x, y, z_b, \lambda)|^4 dx dy}{\int \int_{A_{\text{cell}}} |E(z_m, \lambda)|^4 dx dy}, \quad (1)$$

where the quantity $|E(x, y, z_b, \lambda)|^4$ integrated over the top layer of the unit cell is assumed to be proportional to the TPL signal from the array and compared to $|E(z_m, \lambda)|^4$ integrated over the same size of area, but from a smooth gold film without particles. Using simulated intensity enhancement maps, similar to those shown in Fig. 4 but obtained for several excitation wavelengths, it is possible to estimate the spectral dependence of the achievable TPL enhancement.

The intensity enhancement values estimated from the simulations are shown in Fig. 5, exemplarily in the wavelength range of 480–950 nm for the arrays with $d_x=d_y=150$ nm and $\Lambda_x=\Lambda_y=860$ nm (solid line) and $\Lambda_x=\Lambda_y=740$ nm (dotted line). The TPL enhancement factor roughly resembles the spectral features in the reflection spectra, i.e., a broad peak at ~ 575 nm corresponding to the LSP mode but slightly shifted to the red compared to the dip in the extinction spectrum (see Fig. 1) and peaks at 635 nm (solid line) corresponding to the excitation of the $[1\ 1]$ SPP mode and at 880 nm (solid line) and 750 nm (dotted line), respectively, corresponding to the excitation of the $[1\ 0]$ SPP mode.

Also for the other arrays investigated up to here (TPL spectra not shown), the major contribution to the TPL signal is predicted to be at ~ 575 nm. We have noted previously that the LSP resonance wavelengths deduced from the reflec-

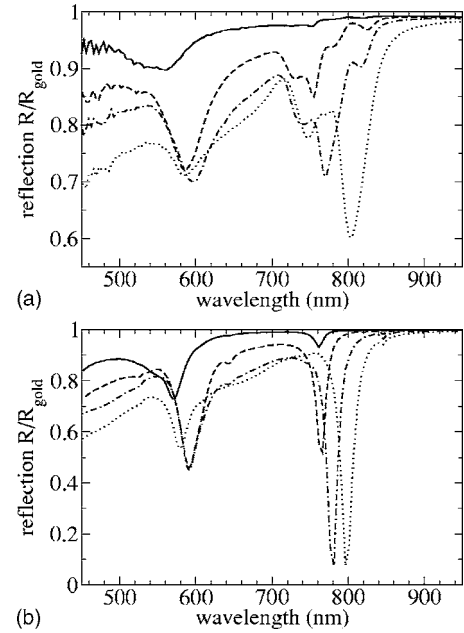


FIG. 6. (a) Measured and (b) calculated reflection spectra of particle arrays with $\Lambda_x=760$ nm, $\Lambda_y=750$ nm and $d_x=d_y=160$ nm (solid line), $d_x=d_y=265$ nm (dashed line), $d_x=d_y=364$ nm (dash-dotted line), and $d_x=d_y=465$ nm (dotted line). The particle height is $d_z=50$ nm and the polarization is parallel to y .

tion and/or extinction (far-field) spectra might differ from the TPL enhancement maxima found from near-field calculations.¹⁰ In the current case, the redshift might be due to the circumstance that the reflection dip is associated with the absorption of the resonantly excited LSP mode (and the absorption drastically increases toward shorter wavelengths), whereas the TPL enhancement peaks at the maximum of the LSP field.

D. Measured TPL enhancement

It transpires from the preceding considerations that the insofar investigated arrays are not expected to lead to strong TPL enhancements or significant spectral features in the experimentally accessible spectral range between 730 and 820 nm (Fig. 5). Indeed, TPL measurements showed enhancement factors of ~ 10 – 20 , with spectrally flat characteristics (not shown). For a more valuable comparison of simulated and measured TPL signals, it is necessary to investigate arrays exhibiting pronounced (resonant) TPL features in the spectral range accessible to our experimental setup.

In order to design and fabricate an appropriate sample, we first optimized the array parameters by simulations and found that arrays with $\Lambda_x=\Lambda_y \approx 750$ nm (similar to the arrays investigated in the previous section) and particle dimensions close to $d_x=d_y \approx 400$ nm should have a relatively strong resonance associated with the $[1\ 0]$ SPP excitation in the spectral region relevant to the experiment [Fig. 6(b)]. The reflection spectra of the correspondingly fabricated sample [Fig. 6(a)] exhibit close similarities to the simulations, except for the experimentally observable much stronger occurrence of the dip attributed to the excitation of light scattered

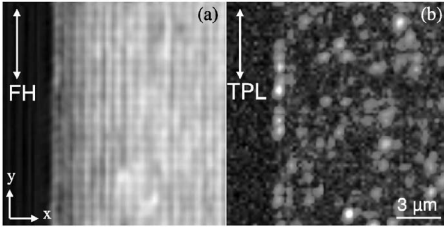


FIG. 7. (a) FH and (b) TPL image of a gold particle array with $\Lambda_x=760$ nm, $\Lambda_y=750$ nm, and particle size $d_x=d_y=465$ nm and $d_z=50$ nm obtained using ~ 0.3 mW of incident power at the wavelength of 745 nm. The maximum TPL signal is ~ 1600 cps and the polarization of excitation and detected TPL is parallel to y , as indicated by the arrows on the images.

at grazing angle to substrate (a close analysis of the simulated spectra reveals also the presence of this feature but as a very weak shoulder of the $[1\ 0]$ -grating coupling dip). This difference as well as the weaker and broader experimentally observed dips compared to the simulations were already observed with the previous samples and can be explained similarly (Sec. III A).

We have experimentally investigated TPL from the arrays with particle sizes $d_z=50$ nm and $d_x=d_y=160, 265, 364,$ and 465 nm for polarization parallel to y and seven different wavelengths (730, 745, 760, 775, 790, 805, and 820 nm), recording reflected fundamental harmonic (FH) and TPL microscopy images.¹⁰ The typical FH and TPL images obtained from the area with 465-nm-sized particles are displayed in Fig. 7 for the excitation wavelength of 745 nm. For every wavelength, the FH and TPL images were obtained starting at ~ 3 μm outside the array of particles. This relatively long distance was used in order to get an accurate reference from smooth gold surface areas. Note that the FH images have been recorded in the cross-polarized configuration. This means that the smooth gold film (reflecting the FH radiation with the maintained polarization) will appear dark in the FH images, while the gold particles (scattering and changing the light polarization) will appear bright.

Applying the method used previously,^{8,10,12} the intensity enhancement factor α observed in the TPL measurements can be estimated by comparing the area averaged TPL signals from the arrays to those from smooth gold films. The used relation is

$$\alpha = \sqrt{\frac{S_{\text{array}} \langle P_{\text{film}} \rangle^2 A_{\text{film}}}{S_{\text{film}} \langle P_{\text{array}} \rangle^2 A_{\text{array}}}}, \quad (2)$$

where S is the obtained TPL signal, $\langle P \rangle$ is the used average incident power, and A is the area generating the TPL signal. The average TPL enhancement estimated from the recorded TPL images using this relation is shown in Fig. 8 as a function of the FH wavelength for all four investigated samples along with the calculated values of the TPL enhancement. It is clearly seen from the experimental results that the array with $d_x=d_y=465$ nm produces the highest average TPL enhancements of ~ 100 , whereas the arrays with smaller particle sizes result in lower enhancements, with their peak positions moving toward shorter wavelengths. A qualitatively

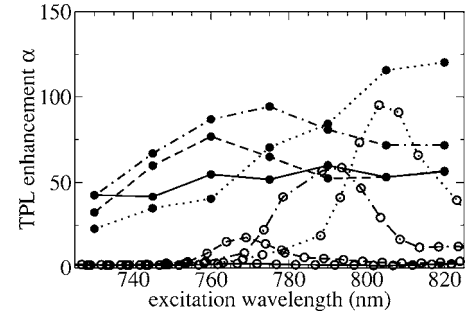


FIG. 8. Measured (filled circles) and calculated (open circles) spectral dependence of the average TPL enhancement [Eq. (2)] obtained from the particle arrays with $\Lambda_x=760$ nm, $\Lambda_y=750$ nm, and $d_x=d_y=160$ nm (solid lines), $d_x=d_y=265$ nm (dashed lines), $d_x=d_y=364$ nm (dash-dotted lines), and $d_x=d_y=465$ nm (dotted lines). The particle height is $d_z=50$ nm.

similar behavior can be observed in the enhancement spectra calculated with the FDTD approach.

It should be mentioned that the maximum TPL enhancement observed from a few individual particles in the array, behaving differently from the average nanoparticles, is ~ 225 . However, at the same time, these few particles (bright spots in the TPL images) seem to be more sensitive to damage and/or reshaping than the remaining particles. Since we aim here at the evaluation of reproducible field enhancements, this damage and reshaping of particularly luminous (individual) positions is neglected in order to allow the excitation power necessary to observe reliable TPL signals from average nanoparticles in the arrays. Note that the incident power used here is between ~ 0.3 and 0.6 mW for the largest particles ($d_x=d_y=465$ nm, $d_x=d_y=364$ nm) and up to ~ 1.7 mW for the smallest particles ($d_x=d_y=265$ nm, $d_x=d_y=160$ nm). These values should be compared to ~ 3 mW used in the previous TPL measurements from arrays with gold particles on glass.¹⁰

One can further observe that, except for the smallest particle size, the measured maximum TPL enhancements actually agree with the calculation results within a factor of 2. However, the experimental TPL peaks are broader and less pronounced as compared to the calculated ones, a difference, which is consistent with the tendency observed when comparing measured and simulated reflection spectra. Additionally, the experimental results might be affected by the circumstance that the TPL signals, being very weak, exhibit considerable uncertainties, especially for longer wavelengths, due to inaccuracy in the focus adjustment, possible gradual damage of the sample, etc. The fact that the TPL enhancement levels measured far from the resonances (especially for the $d_x=d_y=160$ -nm-particle array) do not approach unity should be related to the TPL response from corrugated surfaces (here, due to the surface processing when fabricating particles), which will always be larger than that from the flat surface. The observed difference with the simulations might be due to the fact that the TPL measurements use a tightly focused beam with a (correspondingly) wide angular spectrum. This can result in both broadening of the peaks and increasing of the background by facilitating the SPP excitation at about any wavelength in our wavelength range

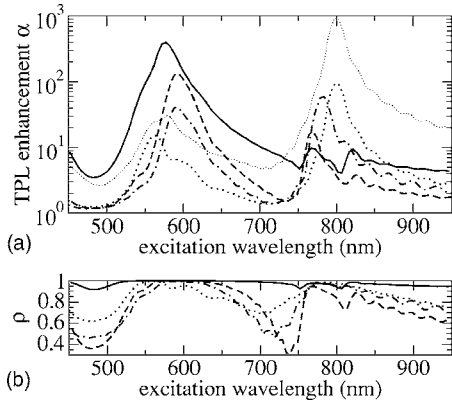


FIG. 9. (a) Average TPL enhancement α and (b) relative contribution ρ of the particle area to the overall TPL signal for arrays with $\Lambda_x=760$ nm, $\Lambda_y=750$ nm, and $d_x=d_y=160$ nm (solid line), $d_x=d_y=265$ nm (dashed line), $d_x=d_y=364$ nm (dash-dotted line), and $d_x=d_y=465$ nm (dotted line). The particle height for all arrays is $d_z=50$ nm and the polarization is parallel to y . The thin dotted line in part (a) depicts the enhancement factor α calculated on the air side of the gold-air interface of the array with $d_x=d_y=465$ nm.

(contrary to what one has in simulations). Moreover, the TPL radiation originating from gold areas with strong field enhancements interacts with the scattering system (i.e., particle array), so that the detected TPL is, in fact, also subject to all scattering phenomena (e.g., LSP and SPP resonances) considered above for the illuminating (FH) radiation. These effects are not accounted for in the simulations of the FH field enhancement and thereby constitute another source of differences between the experimental and calculated TPL enhancement spectra.

Finally, let us elucidate the issue of spatial confinement of the TPL signals and field enhancement. In particular, considering the near-field intensity distributions in Fig. 4, the question on the effective surface zone responsible for the TPL signal arises, i.e., if it is the particle alone that emits the TPL signal. This issue can be clarified by plotting $\rho=S_{\text{part}}/S_{\text{tot}}$, the relative contribution of the simulated TPL signal originating from the particle surface only (S_{part}) to the simulated total TPL signal (S_{tot}) as a function of the excitation wavelength (Fig. 9). It transpires that although the peak at about 800 nm comes from the SPP excitation (i.e., related to delocalized SPP fields), the TPL originates primarily from the particles whenever the enhancement factor α is of considerable strength. The reason for this is that the excited SPPs provide additional “illumination” of the particles (particularly around the edges), which are then responsible for the TPL and near-field enhancement inside the gold. To emphasize the relation of the near-field enhancements on both sides of the gold-air interface, in Fig. 9, we additionally depict for comparison the unit-cell average of the enhancement factor α calculated over a layer just *above* the gold surface (which reflects, e.g., the gain in surface-enhanced Raman

scattering) for the array with $d_x=d_y=465$ nm (thin dotted curve). As can be seen in the graph, it roughly reproduces the general shape of the average TPL enhancement below the gold surface (dotted curve), but is larger by 1 order of magnitude. As discussed in detail in Sec. III B, this is due to the continuity relations, which require a jump of the electric-field component perpendicular to the surface.

IV. CONCLUSION

In conclusion, we have investigated field-enhancement effects in regular arrays of rectangular gold nanoparticles placed on gold films by using reflection spectroscopy and TPL microscopy in combination with FDTD simulations. The dimensions of the nanoparticles and the array periods were systematically varied to optimize the strength of the SPP resonance in the wavelength range accessible to the experimental characterization techniques. On the optimized array, we observed the TPL enhancement up to ~ 200 with a relatively broad spectral response. It could be demonstrated that TPL enhancement is well described by our simulations where we assume that it is related to the field intensity enhancement just below the gold surface, i.e., inside the gold. We could show that even if the optimized resonance at ~ 800 nm is due to a resonant excitation of a delocalized SPP mode, the maximum field enhancement (and thereby the origin of the TPL signal) is localized at the particles. This is due to a combination of geometrical field enhancement (lightning rod effect) and the better penetration of the field into the metal at the particle edges. Additionally, our simulations reveal that the enhancement factor calculated just outside the gold (as it would be probed e.g., by, surface-enhanced Raman scattering) is, on average, one order of magnitude larger than that calculated inside the gold. The origin of this can be found in the continuity relation across the gold-air interface, which requires the electric-field component perpendicular to the interface to be enhanced by the ratio of the dielectric functions.

The obtained results not only give a detailed view of electromagnetic TPL enhancement in gold nanoparticle arrays but also demonstrate the predictive quality of our modeling approach. Moreover, we believe that the results obtained can be further exploited in the ever going search for configurations ensuring reliable realization of strongly enhanced local fields for purposes of surface spectroscopy and (bio-) sensing.

ACKNOWLEDGMENTS

The authors acknowledge support from the European Network of Excellence, Plasmo-Nano-Devices (FP6-2002-IST-1-507879), the STREP “Surface Plasmon Photonics” (FP6-NMP4-CT-2003-505699), the NABIIT project (Contract No. 2106-05-033 from the Danish Research Agency), and the Spanish Ministry of Education and Science (Grant No. MAT2005-06608-C02).

- ¹P. Muhlschlegel, H.-J. Eisler, O. J. F. Martin, B. Hecht, and D. W. Pohl, *Science* **308**, 1607 (2005).
- ²S. Nie and S. R. Emroy, *Science* **275**, 1102 (1997).
- ³J. Azoulay, A. Débarre, A. Richard, and P. Tchénio, *J. Microsc.* **194**, 486 (1999).
- ⁴U. Kreibig and M. Vollmer, *Optical Properties of Metal Clusters*, Springer Series in Materials Science Vol. 25 (Springer, Berlin, 1995).
- ⁵H. Raether, *Surface Plasmons on Smooth and Rough Surfaces and on Gratings*, Springer Tracts in Modern Physics Vol. 111 (Springer-Verlag, Berlin, 1988).
- ⁶N. Féridj, J. Aubard, G. Lévi, J. R. Krenn, G. Schider, A. Leitner, and F. R. Aussenegg, *Phys. Rev. B* **66**, 245407 (2002).
- ⁷B. Lamprecht, G. Schider, R. T. Lechner, H. Ditlbacher, J. R. Krenn, A. Leitner, and F. R. Aussenegg, *Phys. Rev. Lett.* **84**, 4721 (2000).
- ⁸P. J. Schuck, D. P. Fromm, A. Sundaramurthy, G. S. Kino, and W. E. Moerner, *Phys. Rev. Lett.* **94**, 017402 (2005).
- ⁹M. R. Beversluis, A. Bouhelier, and L. Novotny, *Phys. Rev. B* **68**, 115433 (2003).
- ¹⁰A. Hohenau, J. R. Krenn, J. Beermann, S. I. Bozhevolnyi, S. G. Rodrigo, L. Martin-Moreno, and F. Garcia-Vidal, *Phys. Rev. B* **73**, 155404 (2006).
- ¹¹M. A. McCord and M. J. Rooks, *Handbook of Microlithography, Micromachining and Microfabrication* (SPIE and Institute of Electrical Engineers, Bellingham, WA, 1997), Vol. 1.
- ¹²J. Beermann and S. I. Bozhevolnyi, *Phys. Status Solidi C* **2**, 3983 (2005).
- ¹³J. Beermann, S. I. Bozhevolnyi, K. Pedersen, and J. Fage-Pedersen, *Opt. Commun.* **221**, 295 (2003).
- ¹⁴L. Zhao and A. C. Cangellaris, *IEEE Trans. Microwave Theory Tech.* **44**, 2555 (1996).
- ¹⁵A. Taflov and S. Hagness, *Computational Electrodynamics: The Finite-Difference Time-Domain Method* (Artech House, Boston, 2000).
- ¹⁶R. J. Luebbers, *IEEE Trans. Antennas Propag.* **40**, 1297 (1992).
- ¹⁷J. J. Burke, G. I. Stegeman, and T. Tamir, *Phys. Rev. B* **33**, 5186 (1986).
- ¹⁸H. F. Arnoldus, *J. Opt. Soc. Am. A* **22**, 190 (2005).
- ¹⁹J. R. Krenn, H. Ditlbacher, G. Schider, A. Hohenau, A. Leitner, and F. R. Aussenegg, *J. Microsc.* **209**, 167 (2003).